International Journal of Applied Earth Observations and Geoinformation 103 (2021) 102517

Contents lists available at ScienceDirect

International Journal of Applied Earth Observations and Geoinformation

journal homepage: www.elsevier.com/locate/jag

Uncertainty analysis of SVD-based spaceborne far–red sun-induced chlorophyll fluorescence retrieval using TanSat satellite data

Shilei Li, Maofang Gao *, Zhao-Liang Li, Sibo Duan, Pei Leng

Key Laboratory of Agricultural Remote Sensing, Ministry of Agriculture and Rural Affairs/Institute of Agricultural Resources and Regional Planning, Chinese Academy of Agricultural Sciences, Beijing 100081, China

ARTICLE INFO

Keywords:
Singular value decomposition (SVD)
Sun-induced chlorophyll fluorescence (SIF)
TanSat satellite

ABSTRACT

The singular value decomposition (SVD) method, a sun-induced chlorophyll fluorescence (SIF) retrieval approach, has been used widely in far-red SIF spaceborne retrievals on a global scale. However, due to its semi-empirical nature, setting different parameter values may affect its retrieval accuracy, and ultimately have a large impact on its application. Hence, in this study, we evaluated the impact of parameter selection on the far-red SIF retrieval of this approach using TanSat satellite data. We first retrieved the far-red SIF within a narrow spectral window of 757.4–759.2 nm using the first four singular vectors (SVs) that were derived from the snow and soil spectra in a globally distributed training set. The retrievals are highly consistent with TanSat mission SIF ($R^2 = 0.72$), indicating the reliability of our retrieval results. Then, the uncertainty was executed based on the above SIF retrievals and evaluated from five metrics: the number of SVs, length of the fitting window, type of training set elements, proportion of training set elements, and spatial distribution of the training set. Results showed that an unwise selection of the number of SVs would result in large retrieval errors ($R^2 = 0.03$). Meanwhile, a fitting window that is too short or does not include a strong Fraunhofer line would cause severe errors and a large number of negative values ($R^2 = 0.06$). Further, failure to include training samples below the equatorial zone in the Southern Hemisphere, and high latitude samples in the Northern Hemisphere, leads to poorer outcomes ($R^2 = 0.57$). In contrast, the other global sampling metrics had little effect on the retrieval results (generally, $R^2 > 0.97$). Accordingly, the relevant suggestions for using this method in the future are listed in this study for reference, with the potential to improve the accuracy of SIF retrievals from ultra-high spectral resolution instruments in the far-red spectrum.

1. Introduction

Sun-induced chlorophyll fluorescence (SIF) is an electromagnetic signal emitted by chlorophyll molecules after the absorption of visible wavelengths of the solar radiation (Damm et al., 2014; Yang et al., 2015). SIF comes from that part of the energy absorbed by chlorophyll not used for carbon fixation, and instead is reemitted at longer wavelengths in the spectral region of 650–800 nm (Mohammed et al., 2019; Porcar-Castell et al., 2014). As SIF originates at the core of the photosynthetic process, it responds instantly to disturbances in environmental conditions such as changes in light intensity and humidity (Guanter et al., 2012). This makes it more of a direct indicator than reflectance-based vegetation indices of plant photosynthetic activity (Coops et al., 2010; Liu et al., 2019). Recently, various studies on the relationship between SIF and vegetation gross primary production (GPP) have shown that space-based SIF has great application potential in the detection of global photosynthesis (Damm et al., 2015; Goulas et al., 2017; Wei et al., 2018; Zhang et al., 2018b).

Further related research has developed SIF retrieval algorithms using datasets acquired by ground-based (Cogliati et al., 2015; Grossmann et al., 2018), airborne (Damm et al., 2014; Rascher et al., 2015; Wieneke et al., 2016), and spaceborne platforms (Frankenberg et al., 2011a; Joiner et al., 2013; Joiner et al., 2011; Köhler et al., 2015). Benefitting from advances in sensor technology, the first global SIF map was acquired by the Japanese Greenhouse gases Observing Satellite (GOSAT) (Frankenberg et al., 2011b; Guanter et al., 2012; Joiner et al., 2012). Subsequent studies on SIF retrieval have been undertaken using data from the Orbiting Carbon Observatory-2 (OCO-2) satellite (Frankenberg et al., 2014), the Scanning Imaging Absorption Spectrometer for Atmospheric Chartography (SCIAMACHY) onboard the Envisat platform

* Corresponding author.
E-mail address: gaomaofang@caas.cn (M. Gao).

https://doi.org/10.1016/j.jag.2021.102517
Received 1 April 2021; Received in revised form 18 August 2021; Accepted 22 August 2021
Available online 30 August 2021

(Khosravi et al., 2015), the Global Ozone Monitoring Experiment 2 (GOME-2) optical spectrometer (Joiner et al., 2013; Köhler et al., 2015), the Tropospheric Monitoring Instrument onboard the Sentinel-5 Precursor satellite (TROPOMI) (Guanter et al., 2015; Köhler et al., 2018), and the Chinese carbon dioxide observation satellite (TanSat) (Du et al., 2018; Li et al., 2018). Among the various data-driven SIF retrieval approaches involved in the above studies, the singular value decomposition (SVD)-based spaceborne SIF retrieval approach has been used widely as the operational algorithm for global far-red SIF products (Du et al., 2018; Frankenberg et al., 2014; Guanter et al., 2012). These SIF products are retrieved in different spectral windows, such as centered on the Fe line at 758 nm and a KI line at 770 nm.

Generally, data-driven SIF retrieval approaches can be divided into two categories: PCA-based and SVD-based retrieval approaches. The PCA-based algorithms are mostly used in broad spectral windows (>30 nm) with relatively coarse spectral resolution (~0.5 nm), while taking into account the low-frequency contribution of the atmosphere (i.e., a polynomial with respect to wavelength). The SVD-based spaceborne SIF retrieval approach makes use of the Fraunhofer Lines located in a micro spectral window, as a way to disentangle SIF from the top-of-atmosphere (TOA) radiance, while ignoring the influence of the atmosphere. It was first proposed by Guanter et al. (2012) for far-red SIF retrieval using GOSAT data. Soon after, the data-driven method was employed in the OCO-2 (Frankenberg et al., 2014) and TanSat satellite data (Du et al., 2018). The common approach of these studies is the use of a narrow spectral window (1–3 nm) and ultra-high spectral resolution (<0.05 nm) data in the far-red spectrum. However, the SVD-based spaceborne SIF retrieval approach is a semi-empirical model that is affected greatly by the wavelength placement and choice of the model parameters (Zhang et al., 2018a; Zhang et al., 2017). In comparison with reflected sunlight, the SIF signal is small, which means that there is likely a very large uncertainty in SIF retrieval from satellite data. Currently, uncertainty analyses of SVD-based spaceborne SIF retrieval are based on direct estimation of the retrieval error covariance (Du et al., 2018; Guanter et al., 2012). The quantitative impact of parameter selection during the retrieval process remains unclear. Although the issues regarding the representativeness of the training set have been emphasized repeatedly, there is still no pertinent quantitative analysis of the problem or a comprehensive quantitative analysis of the parameters in the model. Therefore, it is of great theoretical and practical relevance to evaluate the influence of the factors that might affect the accuracy of the SVD data-driven method for SIF retrieval.

The remainder of this paper is organized as follows. The TanSat satellite is introduced in Section 2. The methods are described in Section 3. The results are compared and analyzed in Section 4. The discussion and conclusions of this study are given in Sections 5 and 6, respectively.

2. TanSat satellite

TanSat is the first Chinese global carbon dioxide (CO_2) observation satellite, which was developed jointly by the Chinese Academy of Sciences and the National Meteorological Administration of China and launched in December 2016 (Li et al., 2018). Similar to both GOSAT and OCO-2, TanSat was designed to monitor and detect the atmospheric CO_2 content from space. It is a sun-synchronous satellite that orbits at an altitude of approximately 700 km with an equatorial crossing time near 13:30 local solar time and a revisit period of 16 days (Du et al., 2018; Ran and Li, 2019).

TanSat is equipped with two sensors: the high spectral resolution Atmospheric Carbon Dioxide Grating Spectroradiometer (ACGS) and the Cloud and Aerosol Polarimetry Imager that monitor CO_2 and aerosols, respectively. The ACGS has three sets of similar grating spectrometers for hyperspectral detection of radiation information in three bands: 0.76 μm (the O_2-A band), 1.61 μm (the weak CO_2 band), and 2.06 μm (the strong CO_2 band) (Li et al., 2021). The Cloud and Aerosol Polarimetry Imager is used primarily to detect the scattering effects of clouds and aerosols based on measurements in five broad bands at 0.38, 0.67, 0.87, 1.375, and 1.64 μm. In this study, observations acquired in the O_2-A band were selected to retrieve SIF. The O_2-A band covers a spectral range of 757.4–778.0 nm, with a spectral dimension of 1242 channels. The parameters of the TanSat ACGS are presented in Table 1.

TanSat operates in three observation modes, i.e., the nadir, sunglint, and target modes. Target mode operation stares at the target, which is generally a ground verification site. The glint mode, relative to nadir, has varying east–west offsets, and it may underestimate SIF due to a shaded fraction of the canopy (Frankenberg et al., 2014). Compared to the glint mode, the nadir mode typically provides a slightly higher spatial resolution, and a better signal-to-noise ratio over land (Sun et al., 2018). Measurements acquired in the nadir mode can be used to retrieve SIF (Du et al., 2018). The radiance, observed by the ACGS and stored as L1B level data, is radiometrically calibrated and the corresponding wavelength can be calculated using a dispersion coefficient and the number of spectral channels. The formula can be expressed as follows:

$$\lambda = \sum_{i}^{5} c_i \cdot p^{(5-i)} \tag{1}$$

where λ is the spectral wavelength, c is the dispersion coefficient, i is the number of dispersion coefficient, and p is the channel number of the spectral dimension. An example of the extracted radiance spectrum is shown in Fig. 1.

3. Methods

3.1. The SVD-based satellite data-driven algorithm

The SVD-based spaceborne SIF retrieval approach uses solar Fraunhofer Lines to retrieve SIF, which largely simplifies the satellite-based retrieval of SIF (Mohammed et al., 2019). Its basic idea is that any at-sensor radiance spectrum can be treated as a linear combination of a non-fluorescent radiance spectrum plus the SIF propagated to TOA. There is also another pivotal assumption: the non-fluorescent radiance spectrum can be expressed as a linear combination of the singular vectors (SVs) that describe a non-fluorescent set of measurements (Guanter et al., 2012). Additionally, the SVs, in turn, can be separately derived from radiance spectra that do not contain any vegetation information (Du et al., 2018; Guanter et al., 2012).

Similar to the principal component analysis (PCA) method, the SVD technique is a robust statistical analysis tool for linear systems. Its essence is to decompose a large set of correlated variables into a small set of uncorrelated signals named SVs. Usually, the SVD of an $m \times n$ matrix M (m spectra $\times$ n spectral points) can be expressed as:

$$M = U\Sigma V^T \tag{2}$$

where U is an orthogonal matrix ($m \times n$) containing left-column SVs of M, Σ is defined as a singular matrix ($n \times n$) arranged in descending order of singular values, V is a unitary matrix ($n \times n$) containing its n right-column SVs in its n columns, and T is the transpose operator.

Based on the concept of SVs, assuming that SIF remains constant within a narrow fitting window, Guanter et al. (2012) described the

Table 1
Main parameters of the TanSat ACGS instrument.

Band	O_2-A	Weak CO_2	Strong CO_2
Spectral range (nm)	758–778	1594–1624	2041–2081
Spectral resolution (nm)	0.033–0.047	0.120–0.142	0.160–0.182
Signal-to-noise ratio	360	250	180
Spatial resolution (km)	2 × 2		
Overpass time	1:30 pm		
Revisit time (day)	16		
Swath (km)	20		

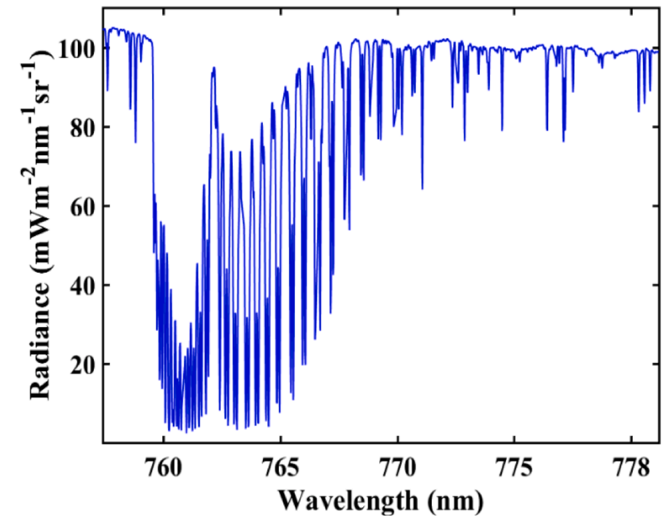

Fig. 1. Example of radiance spectrum acquired by the TanSat ACGS instrument in the vicinity of the O_2-A band, used for SIF retrievals.

radiance detected at the TOA as:

$$F(\omega, F_S) = \sum_{i=1}^{n_v} \omega_i v_i + F_s^{TOA} I \tag{3}$$

where n_v is the number of SVs selected to model the input radiance spectrum, ω_i is the weight of the singular vector v_i, F_s^{TOA} is the intensity of the fluorescence signal at the TOA, and I is a unit column vector of size n. Note that Eq. (3) is the final forward model used to retrieve SIF and to analyze the uncertainty of the SVD-based data-driven algorithm in Section 4.

An example of a reconstructed TOA radiance with or without considering SIF in the forward model using the first four SVs (see Section 3.2) is shown in Fig. 2a. The fittings both with or without the SIF are highly similar to the measured spectrum, indicating the input spectra are modeled correctly. RMSE between all the reconstructed spectra and measured spectra that consider both the retrieved and unretrieved SIF are displayed in Fig. 2b. Results show that the RMSE remarkably decreases when SIF is considered. This error is distributed between 0.03 and 0.08 mW m^{-2} nm^{-1} sr^{-1}, which can be ignored compared with TanSat TOA radiance values.

3.2. Selection of training set and generation of SVs

A training set of non-vegetated land targets was selected to generate the set of SVs. The purpose was to create a training set containing spectra under as many different conditions as possible. Following Du et al. (2018), the selection rules of the vegetation-free spectra include: (1) non-vegetated surface (i.e., bare soil, snow, and water), (2) normalized and averaged at-sensor radiance in the O_2-A band within the range 25–200 mW m^{-2} nm^{-1} sr^{-1}, and (3) uniform longitudinal and latitudinal distribution.

The training spectra were extracted from TanSat global data acquired on seven days (i.e., one day in every five days) in July 2017. This produced a training set of 11,372 pure non-vegetated spectra. The global distribution of the training set is shown in Fig. 3. The effect of the sun zenith angle was eliminated by normalizing the mean radiance in the O_2-A band using the cosine of the sun zenith angle (Du et al., 2018). The selected training set was divided into five categories, the total training set (11,372 spectra), snow and soil (7,597 spectra), snow (3,805 spectra), soil (3,792 spectra), and water (3,775 spectra), to facilitate the uncertainty analysis in Section 4. The snow and soil spectra (the second category) are used in Sections 4.1, 4.2, 4.3 and 4.4.2. The total training set (the first category) and the single element spectra of snow, water, and soil are used in Section 4.4.1, and the mixed spectra of soil and water are used in Section 4.4.3. Note that the second category is the same type as the training set used for the operational TanSat mission SIF product (TanSat SIF).

According to Eq. (2), we generated the SVs that were derived from the total training set. The first six SVs of the 757.4–759.2 nm fitting window are plotted in Fig. 4. The first singular vector accounts for most of the variance of the total training set and it represents the main spectral shape. The second and third SVs mostly contain information about the spectral slope and spectral shift due to Doppler shifts. The fourth singular vector possibly shows the symmetry of the spectrum. More than 99% of the variance is captured by these first four SVs, whereas the variance explained by the fifth and sixth SVs are less than 0.05%. Motivated by Guanter et al. (2012) and Du et al. (2018), an empirical threshold of 0.05%, which explains the percentage of the variance of the training set for each singular vector, was adopted to determine the number of SVs ($n_v$in Eq. (3)). Therefore, we could ignore the information contained by the fifth and sixth SV, or treat them as invalid information. Eventually, we selected the first four SVs (e.g., Fig. 4a–d) to model the TanSat radiance.

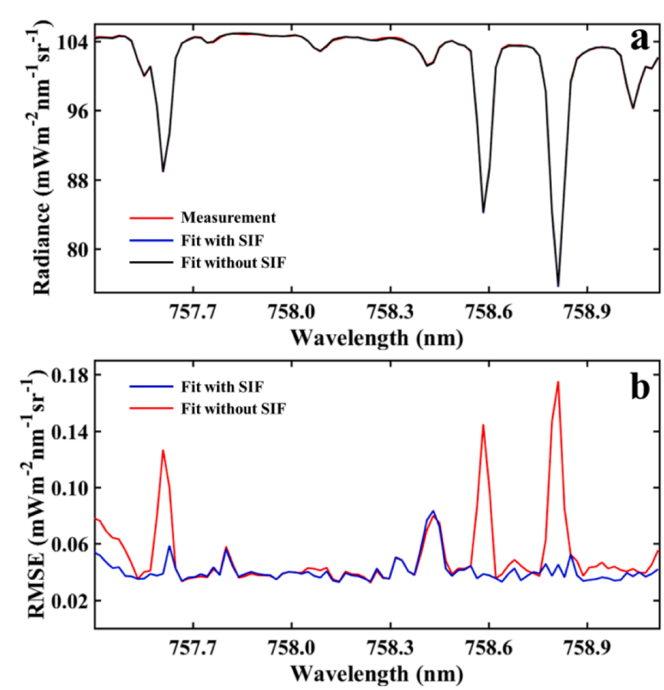

Fig. 2. (a) Example of a reconstructed TOA radiance with or without SIF, and (b) the impact of SIF on the fit illustrated by the difference in RMSE.

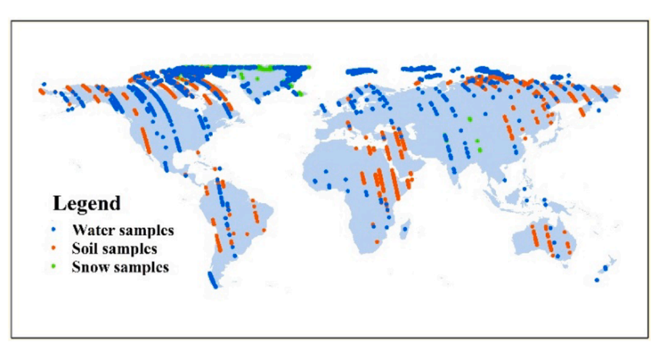

Fig. 3. Spatial distribution of the 11,372 non-vegetated spectra in the training set, including snow, soil, and water samples that are selected from TanSat data.

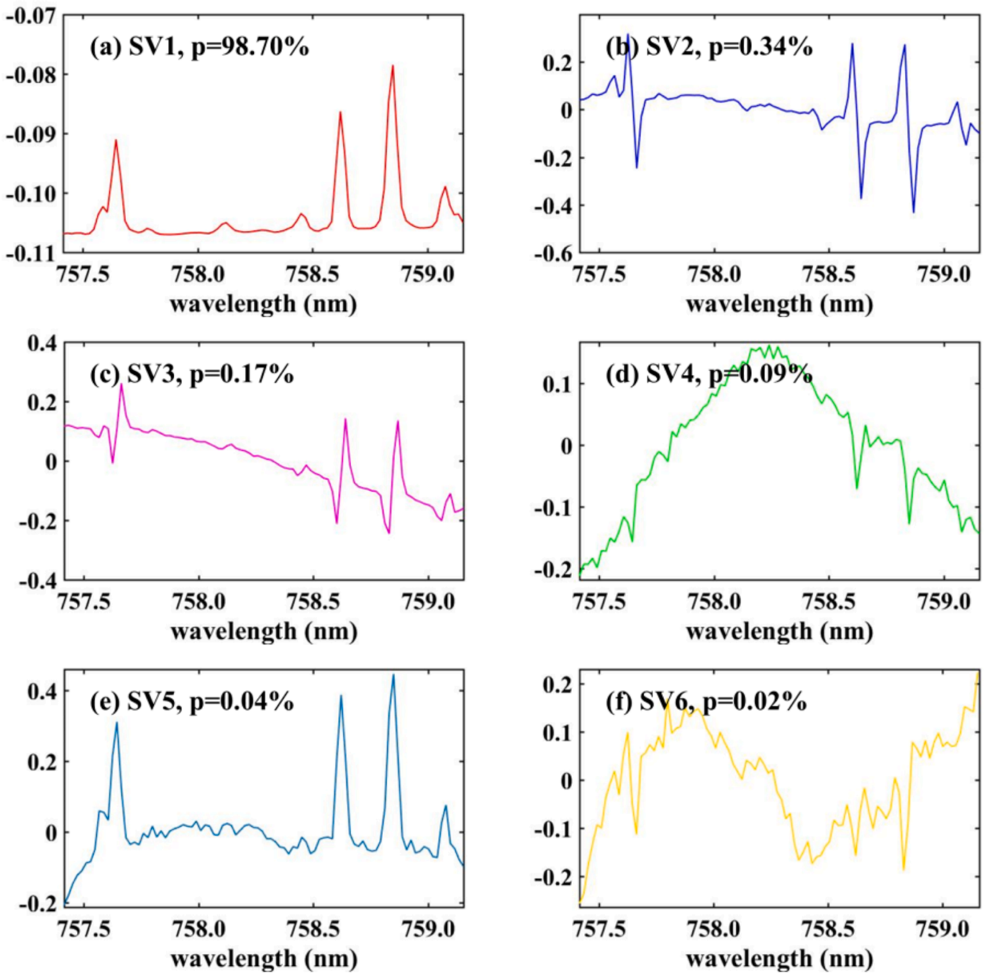

Fig. 4. Spectra obtained for the first six SVs derived from the total training set. Percentages in the panels represent the relative amount of information captured by each singular vector.

3.3. Uncertainty assessment

The uncertainty analysis was mainly carried out by analyzing the SIF retrievals under different parameter settings. Therefore, for the accuracy evaluation, we selected the commonly used statistical parameters, namely, R^2, RMSE and bias. These formulas can be expressed as follows:

$$R^2 = \left(\frac{\sum_{i=1}^{n} \left(SIF_i - \overline{SIF}\right) \bullet \left(SIF_{ri} - \overline{SIF_r}\right)}{\sqrt{\sum_{i=1}^{n} \left(SIF_i - \overline{SIF}\right)^2} \bullet \sqrt{\sum_{i=1}^{n} \left(SIF_{ri} - \overline{SIF_r}\right)^2}} \right)^2 \quad (4)$$

$$RMSE = \sqrt{\frac{\sum_{i=1}^{n} (SIF_i - SIF_{ri})^2}{n}} \quad (5)$$

$$bias = \frac{\sum_{i=1}^{n} (SIF_i - SIF_{ri})}{n} \quad (6)$$

where SIF and SIF_r are the retrieved SIF and reference SIF; $\overline{SIF}$ and $\overline{SIF_r}$ are the averaged values of retrieved SIF and reference SIF, and i and n are the sequence number and the total number of observations, respectively.

4. Results

4.1. Assessment of the SIF retrievals

First, we retrieved far-red SIF from TanSat measurements using the SVD-based spaceborne SIF retrieval approach proposed by Guanter et al. (2012). Then, we set different parameter values during the inversion process and performed multiple retrievals using TanSat data; thereafter, we evaluated the uncertainty of the retrieval results under different parameter settings based on the reference SIF (defined at the end of this section). The training set of the second category (e.g., snow and soil spectra described in Section 3.2) was used to retrieve SIF according to the forward model given by Eq. (3), and the retrieval results were compared with the TanSat SIF and OCO-2 mission SIF product (OCO-2 SIF). It should be emphasized that the dataset of SIF retrievals matches the locations of the TanSat SIF, whereas the distance from the center of the OCO-2 SIF footprint is controlled within 1 km. The spatial distribution of the dataset of SIF retrievals on July 5, 2017 for these two satellites along the same orbit is provided in Fig. 5a.

Fig. 5 shows the good agreement between TanSat SIF and OCO-2 SIF in July 2017. Although the global distribution is highly coordinated, there is still the possibility of local considerable differences (Fig. 6c). Comparisons of our SIF retrievals (N = 18,951) with the TanSat SIF and OCO-2 SIF are shown in Fig. 6. SIF retrievals are correlated strongly with the TanSat SIF with a R^2 of 0.72, whereas the R^2 of the comparisons with the OCO-2 SIF is 0.380 (Fig. 6b) and 0.427 (Fig. 6c). This might be

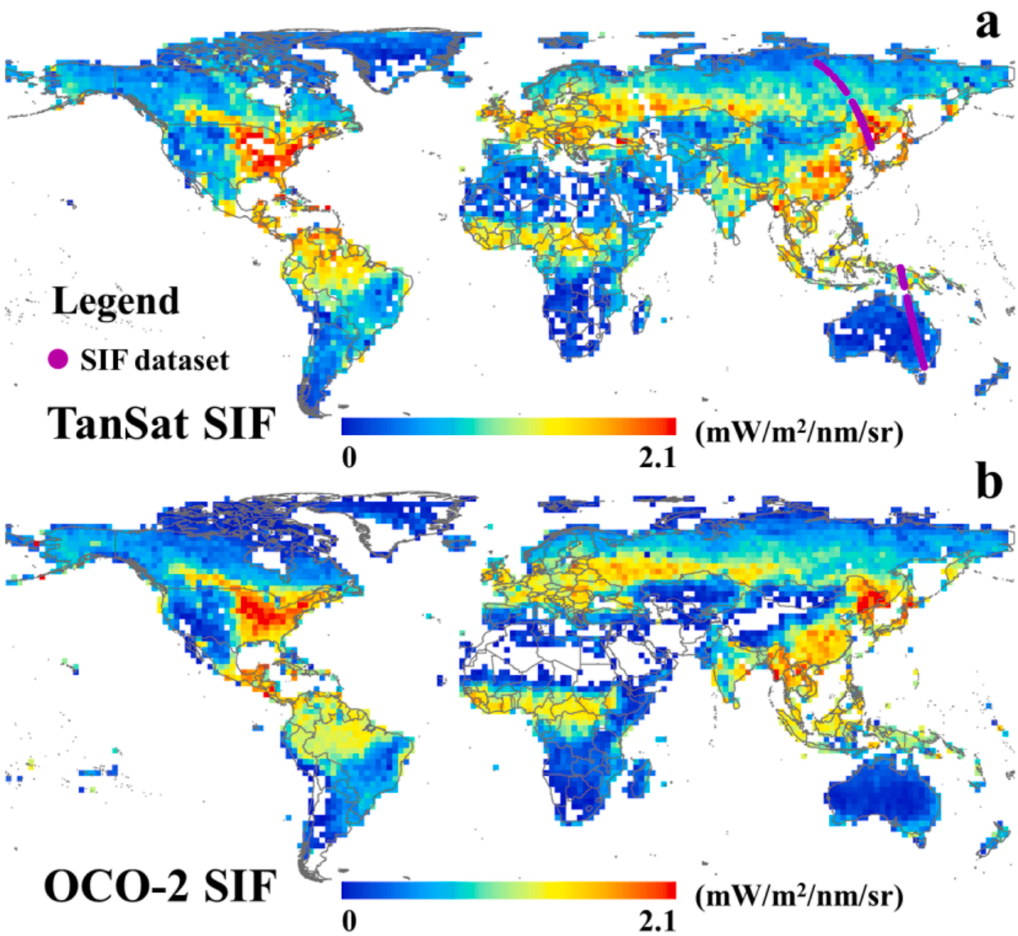

Fig. 5. Global maps of TanSat SIF (a) and OCO-2 SIF at 2° resolution in July 2017. The spatial distribution of the SIF dataset used for comparisons along one orbit is displayed in panel (a).

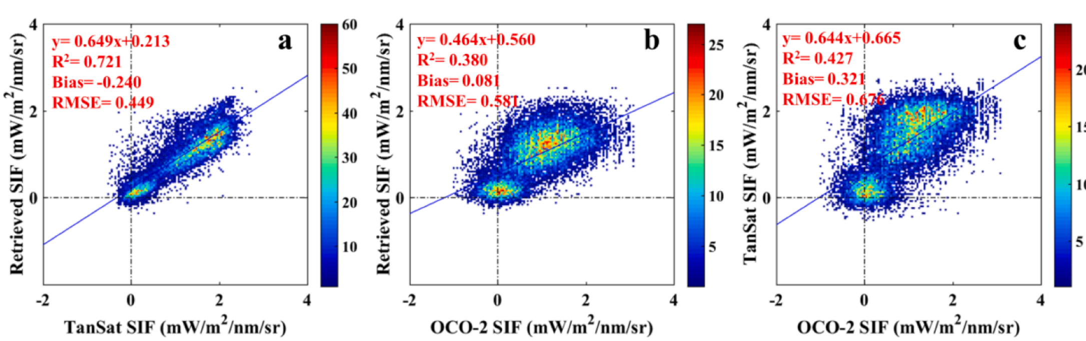

Fig. 6. Comparisons of (a) our SIF retrievals versus the TanSat mission SIF product (TanSat SIF), (b) retrieved SIF versus the OCO-2 mission SIF product (OCO-2 SIF), and (c) the TanSat SIF versus OCO-2 SIF. The color scales in each panel represent a different number of scattered SIF values, increasing from blue to red. The blue and black lines respectively show the fitted lines and reference lines (intersecting lines for zero values) per panel. There are 18,951 SIF values in the reference SIF, due to the selection of adjacent pixels when comparing with OCO-2 SIF. (For interpretation of the references to color in this figure legend, the reader is referred to the web version of this article.)

attributable to the instrument performance, incomplete correspondence of the footprints, and different retrieval methods. Fig. 6 illustrates that SIF retrievals made in this paper, when compared with OCO-2 SIF, slightly underestimate the reported TanSat SIF values (e.g., max SIF of ~2.8 mW/m^2/nm/sr), and neither generates a substantial number of negative SIF values (Fig. 6a). OCO-2 (Fig. 6b) generated many negative SIF cases and overestimated the maximum SIF (as compared to TanSat in Fig. 6a). Consequently, these two mission SIF retrievals only agreed ~43% of the time (Fig. 6c). Owing to the difficulty of authenticity verification, it is hard to directly determine which retrieval is better. Considering the high correlation with TanSat SIF and the lower RMSE with OCO-2 SIF, we decided to assign the SIF dataset retrieved by the training set of the second category (snow and soil samples) as the reference SIF (N = 22,718) with which to evaluate the accuracy of the retrieval results under different parameter settings in the following sections.

4.2. The influence of the number of SVs

The number of SVs is an important component affecting the non-fluorescence spectrum, which is naturally the crucial parameter for SIF retrieval. The number of SVs input into the forward model determines the accuracy of spectral reconstruction and SIF retrieval. One of the objectives of this study is to investigate the influence of the number of SVs on SIF retrieval. Initially, we used the first 1–3 and 5–7 SVs to retrieve SIF and compared the results with retrievals derived by the first 4 SVs. Fig. 7 depicts all the comparisons. It is apparent that the retrieval results are severely affected by the number of SVs. The best agreement between retrieved and reference SIF was achieved with the first three SVs (Fig. 7c), including the maximum SIF obtained (~2.8 $mW/m^2/nm/sr$), which also produced the lowest number of negative SIF values. As the number of SVs increases from SV1 to include SV1-SV3, our retrieval results become closer to the reference SIF (Fig. 7a–c), whereas when the number of SVs exceeds 4, the correlation almost disappears (Fig. 7d–f). Interestingly, although the number of SVs is close, the results differ significantly (Fig. 7d, when compared with the retrieved SIF using the first four SVs). This appears to be attributable to overfitting of the spectra (a detailed discussion is provided in Section 5.2) (Du et al., 2018; Guanter et al., 2012). Therefore, the number of SVs must be carefully determined when using the SVD-based spaceborne SIF retrieval approach.

4.3. The effect of the fitting window length

The fitting window is a spectral range used to retrieve SIF in the forward model. In this study, the reference SIF data were retrieved with a micro spectral range of 757.4–759.2 nm (the original spectral window), which is basically the same as that of the TanSat SIF operational product. To investigate the impact of the fitting window length on the retrieval results, several adjacent spectral windows were selected for comparison. The fitting windows (window lengths, number of channels, numbers of negative values, and percentage of negative values) available are presented in Table 2.

There are 92 channels in our original fitting window, and the comparisons of retrieved and reference SIF are presented in Fig. 8 for the six cases listed in Table 2. The worst agreement occurred for the narrowest fitting window (1.0 nm, Fig. 8f), which also generated a substantial number of negative SIF values. From Fig. 8, our SIF retrievals are more consistent with the reference SIF when the spectral range used was close to the original spectral window (Fig. 8b), and produces the lowest number of negative values (Table. 2). Conversely, as the length of the fitting window continues to increase or decrease, the correlation between the retrieval results and the reference SIF becomes increasingly poorer (Fig. 8a, c–f) and produces a large number of negative SIF values (especially, Fig. e-f). For Fig. 8a, the possible explanation for the decreased correlation is that the spectral window is inserted by the oxygen lines (see Fig. 13), while for Fig. 8e–f, the reason is that the spectral windows are too short. Taken as a whole, the information in this section indicates that the length of the fitting window matters to the SIF retrieval and implies that, for the TanSat satellite, a fitting window between 1.5 and 1.9 nm is optimal in the range between 757.4 and 759.3 nm. Also, short spectral windows (<1.5 nm) will result in a large number of negative values. This is particularly relevant for the narrow fitting window, wherein small changes in the spectral length might lead to a considerable influence on the outcomes.

Table 2
Different fitting windows and their corresponding parameter values.

Figure	Window length (nm)	Number of channels	Number of negative values	Percentage of negative values
8a	757.4–759.5	112	2132	9.38 %
8b	757.4–759.3	101	259	1.14 %
8c	757.5–759.15	85	2719	11.97 %
8d	757.5–759.0	78	3539	15.57 %
8e	757.7–759.0	68	6604	29.07 %
8f	758.0–759.0	52	11,413	50.24 %

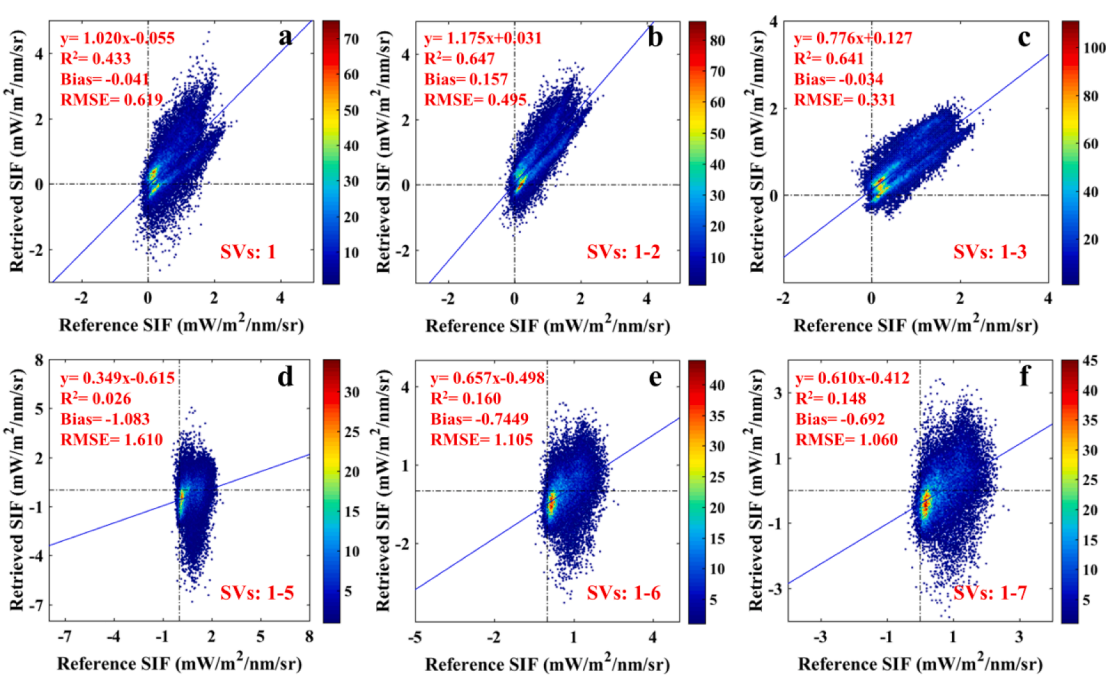

Fig. 7. Retrieval results with selecting the (a) first one singular vector, (b) first two SVs, (c) first three SVs, (d) first five SVs, (e) first six SVs and (f) first seven SVs. The color scales in each panel represent a different number of scattered SIF values, increasing from blue to red. The blue and dark lines show the fitted lines and reference lines (intersecting lines for zero values) per panel. Reference SIF corresponds to the SIF dataset retrieved from TanSat data using the second category of training set, which is defined at the end of Section 4.1. (For interpretation of the references to color in this figure legend, the reader is referred to the web version of this article.)

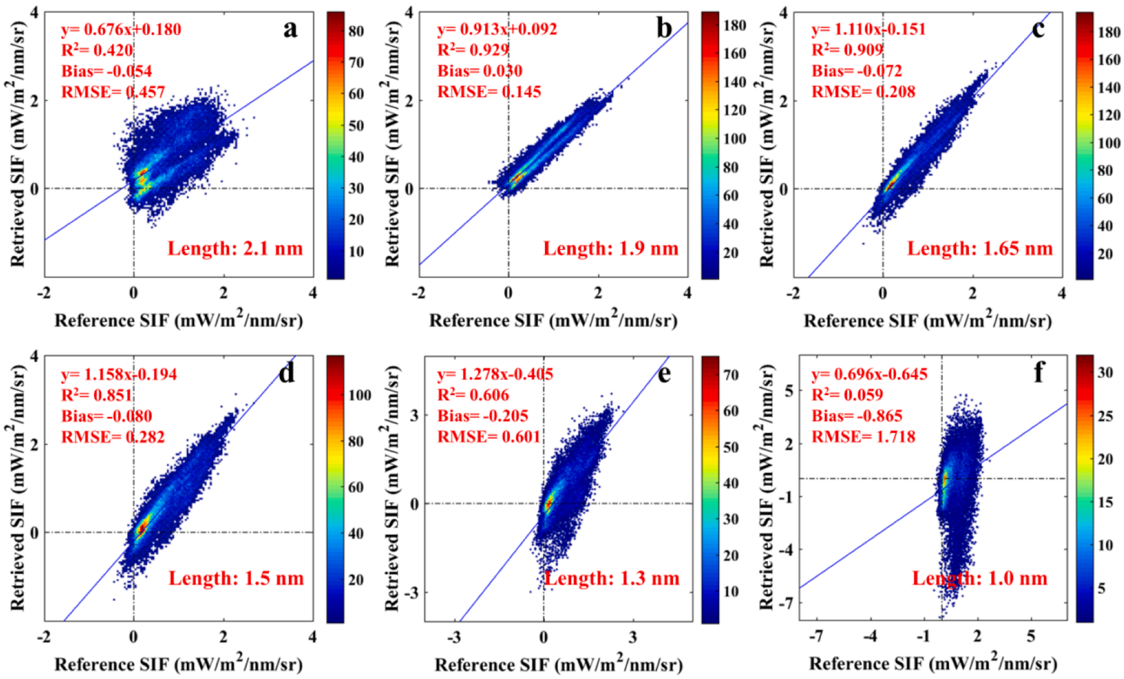

Fig. 8. Retrieval results of different fitting window lengths. The specific correspondence is presented in Table 2. The color scales in each panel represent a different number of scattered SIF values, increasing from blue to red. The blue and dark lines show the fitted lines and reference lines (intersecting lines for zero values) per panel. A large number of negative values occurred for (e) and (f). Note that the data ranges shown are the same for the X and Y scales in (a-d), but are reduced in (e) or expanded for (f). Reference SIF corresponds to the SIF dataset retrieved from TanSat data using the second category of training set, which is defined at the end of Section 4.1. (For interpretation of the references to color in this figure legend, the reader is referred to the web version of this article.)

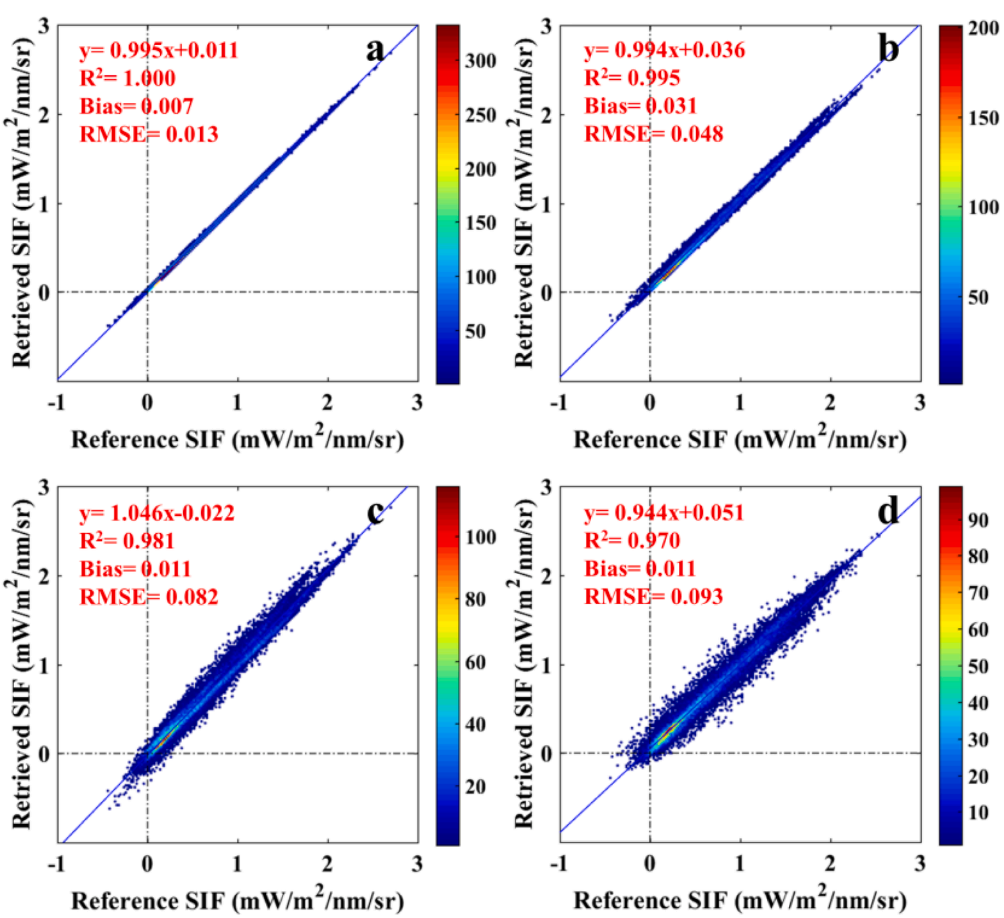

Fig. 9. Retrieval results of (a) the total training set, (b) water spectra, (c) snow spectra, and (d) soil spectra. The color scales in each panel represent a different number of scattered SIF values, increasing from blue to red. The blue and dark lines show the fitted lines and reference lines (intersecting lines for zero values) per panel. Reference SIF corresponds to the SIF dataset retrieved from TanSat data using the second category of training set, which is defined at the end of Section 4.1. (For interpretation of the references to color in this figure legend, the reader is referred to the web version of this article.)

4.4. The impact of the training set

4.4.1. The element type of the training set

Theoretically, there are many types of land covers that do not include vegetation, such as deserts, cloudy oceans, and sea ice (Joiner et al., 2016). We selected available data from the TanSat satellite to evaluate the impact of using different types of training elements on SIF retrieval. The categories of total training set, all snow spectra, all soil spectra, and all water spectra were each used to retrieve SIF and the comparisons with reference SIF are given in Fig. 9. Retrievals are essentially equal when using either water spectra only (Fig. 9b) or when water spectra are combined with snow and soil spectra (Fig. 9a). When using snow spectra to retrieve SIF (Fig. 9c), some results are overestimated slightly. This might be because the snow spectra occur mainly in high latitudes having less global representation. The retrieval results using soil spectra are also close to the reference SIF with $R^2 > 0.97$ and RMSE < 0.1 mW/m^2/nm/sr (Fig. 9d). Therefore, we can conclude from Fig. 9 that SIF can be retrieved with high precision whether utilizing mixed or single-element spectra as the SIF-free representation. However, the premise is that the spectra adopted must be globally representative.

4.4.2. The proportion of training set elements

To analyze the influence of the proportion of training set elements on the retrieval results, we filtered the snow and soil spectra by latitude to approximately 1/2 (1801 snow spectra & 1879 soil spectra) and 1/3 (1229 snow spectra & 1226 soil spectra) of the original numbers (our rules: retain one per every two or three on the original training set). After filtering, the training set changed little in the longitudinal range, but became sparse in the latitudinal direction. Comparisons are presented in Fig. 10. As the number of elements in the training set were 1/3 and 1/2 of the original numbers (Fig. 10a and b), the retrieval results are slightly overestimated compared with the reference SIF, which could be attributable to a little loss of latitudinal representativeness. Whether it is snow or soil that dominates the spectra in the training set, as long as another type of spectra (soil or snow) is mixed, the retrieved SIF and the reference SIF maintain a high degree of consistency, with all $R^2 > 0.99$ and RMSE < 0.1 mW/m^2/nm/sr (Fig. 10 c–f). This not only indicates that the influence of the proportion of training set elements is extremely small (or can be ignored) when the distribution of the training set is globally representative, but also fits the conclusion of the previous section: as the single-element spectra can be used to retrieve SIF, and there is no further need to consider the proportion of the mixed spectra.

4.4.3. The spatial distribution of the training set

As stated in Section 4.4.1, single-element spectra can be used to retrieve SIF. To investigate the influence of an uneven spatial distribution of the training set on the retrieval results, we selected mixed spectra that containing soil and water samples as the new training set to retrieve SIF. Our rationale is that soil and water spectra are distributed uniformly across the globe and the sum of their numbers is large enough for our analyses.

We evaluated the effect of an uneven distribution of the training set on SIF retrievals from two aspects: longitude and latitude. The longitudinal and latitudinal ranges corresponding to the training set and the associated numbers of training samples are displayed in Table 3. A comparison of the results is depicted in Fig. 11. The subfigures of a–d and e–h represent the results retrieved based on training sets with different latitudinal and longitudinal ranges, respectively. It can be seen that when the latitudinal range changes and with larger training sets, the

Table 3
Longitudinal/latitudinal distribution of different training sets.

Figure	Latitudinal range	Number of training sets	Figure	Longitudinal range	Number of training sets
11a	5°S–57°N	1613	11e	38°W–40°E	1642
11b	24°S–73°N	3445	11f	71°W–70°E	3519
11c	34°S–81°N	5418	11 g	102°W–101°E	5567
11d	37°S–82°N	7343	11 h	164°W–163°E	7371

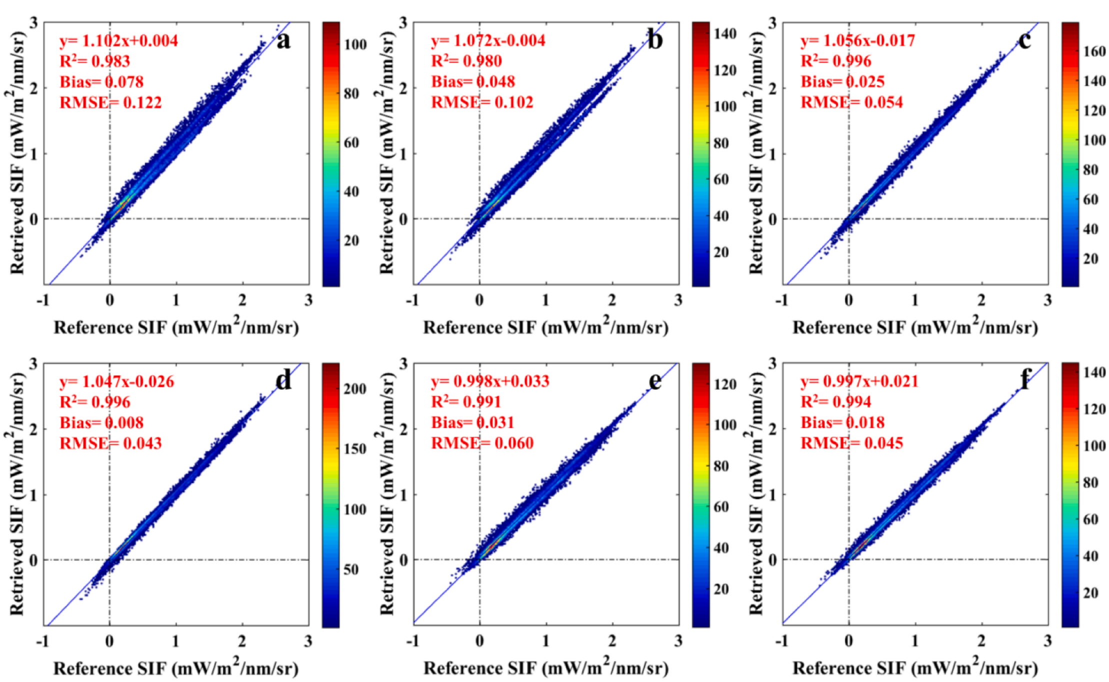

Fig. 10. Retrieval results of (a) 1/3 snow and 1/3 soil spectra, (b) 1/2 snow and 1/2 soil spectra, (c) all snow and 1/3 soil spectra, (d) all snow and 1/2 soil spectra, (e) 1/3 snow and all soil spectra, and (f), 1/2 snow and all soil spectra. The color scales in each panel represent a different number of scattered SIF values, increasing from blue to red. The blue and dark lines show the fitted lines and reference lines (intersecting lines for zero values) per panel. Reference SIF corresponds to the SIF dataset retrieved from TanSat data using the second category of training set, which is defined at the end of Section 4.1. (For interpretation of the references to color in this figure legend, the reader is referred to the web version of this article.)

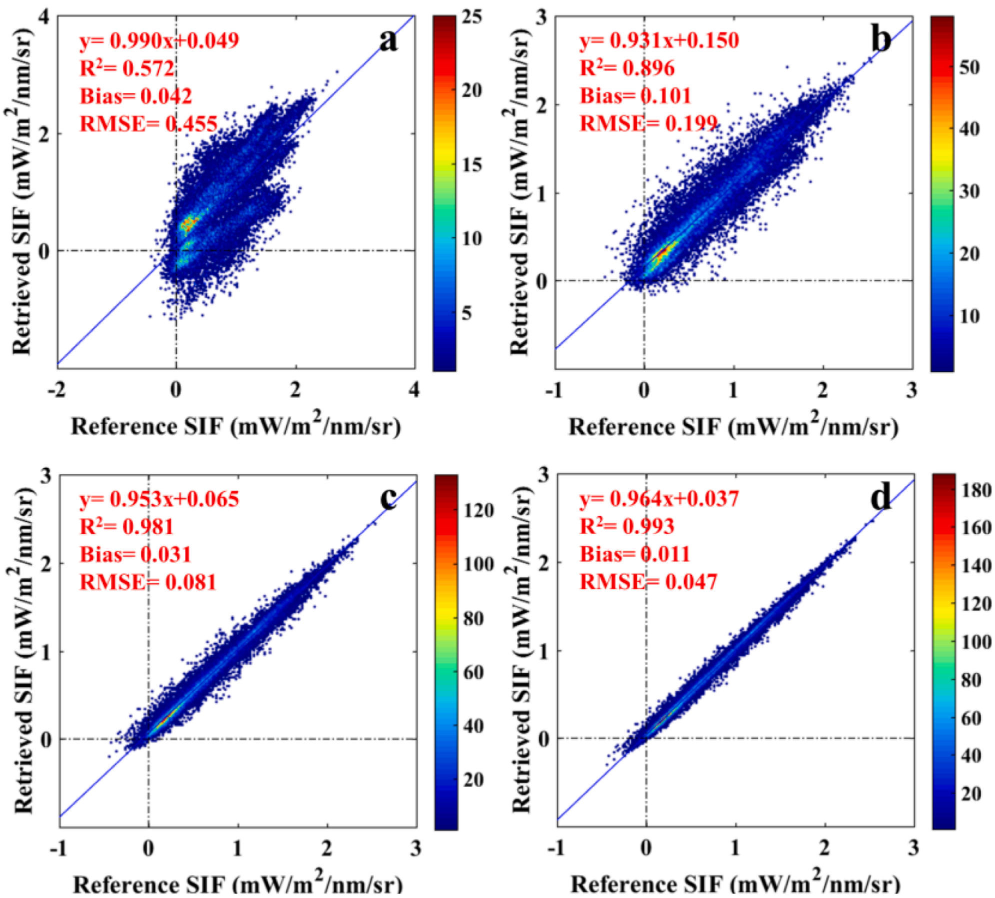

Fig. 11. Retrieval results of training sets (a)–(d) with different latitudinal ranges and (e)–(h) different longitudinal ranges. The specific correspondence is shown in Table 3. The color scales in each panel represent a different number of scattered SIF values, increasing from blue to red. The blue and dark lines show the fitted lines and reference lines (intersecting lines for zero values) per panel. Reference SIF corresponds to the SIF dataset retrieved from TanSat data using the second category of training set, which is defined at the end of Section 4.1. (For interpretation of the references to color in this figure legend, the reader is referred to the web version of this article.)

retrieval results differ significantly. In particular, the lack of training samples in high-latitude regions in the Northern Hemisphere and below the equatorial zone in the Southern Hemisphere leads to large differences in retrieval results and generates a noticeable number of negative SIF values (Fig. 11a). The larger the latitude covered by the training set, the closer the retrieval is to the reference SIF (Fig. 11b–d). A possible explanation for this might be that a small latitude coverage (approximately 62 latitudes, see Table 3) will lead to insufficient global representation of the training set, resulting in poor accuracy of the outcomes. In contrast, despite similar coverage changes occurring across longitudes, the retrievals remained close to the reference SIF (Fig. 11e–h). Overall, these results suggest that the influence of the latitudinal distribution of the training set is greater than that of the longitudinal distribution, and the training set should sample the globe as much as possible when using the SVD-based method to retrieve SIF from satellite data.

5. Discussion

5.1. The inspiration of this study

The core of the data-driven algorithms that are used for SIF retrievals rely on the feature extraction of many non-fluorescence target spectra. The extracted features can then be applied to separate the SIF signal on the basis of a simplified radiative transfer model.

The PCA-based SIF retrieval approach has been used for SIF retrieval near the O_2-A band (Joiner et al., 2013; Köhler et al., 2015; Sanders et al., 2016) and the O_2-B band (Joiner et al., 2016) based on GOME-2 and SCIAMACHY satellite data. The corresponding sensitivity analysis is performed with simulated data of the matrix operator model radiative transfer code (Fell and Fischer, 2001) from the perspectives of the number of principal components (PCs), signal-to-noise ratio, fitting window length, instrumental noise, and spectral resolution. The above analysis regarding the PCA-based SIF retrieval approach represents important work. However, these analyses are based on simulated data and lack a description on the sensitivity of the algorithm to the training set. The usage of Fraunhofer Lines significantly simplifies the satellite-based retrieval of SIF; however, the relative SIF signal is relatively much lower in these very narrow lines compared with the O_2 bands. With Fraunhofer lines, larger retrieval uncertainties occur, although that might not play a major role when seasonal time series characterized by an abrupt change from non-vegetation to full vegetation cover are analyzed. But, this issue might prevent more detailed analysis to understand smaller changes of SIF caused by environmental stress conditions (Mohammed et al., 2019). While it has been common to directly evaluate the SVD-based SIF retrieval errors using the error covariance matrix (Du et al., 2018; Frankenberg et al., 2014; Guanter et al., 2012). However, certain key factors that might affect the results have been ignored, which could represent a notable drawback. Given that no comprehensive uncertainty analysis on this SVD-based method has been reported, the specific objective of this study is to investigate the impact of the training set, length of fitting window, and the number of SVs on SIF retrieval. The specific five aspects have been described in Section 4.

5.2. Determine the number of SVs

The determination of the optimal number of SVs is a critical step for the far-red SIF retrieval using the SVD-based approach. Previous reports have shown that 0.05% is the insurance threshold for selecting SVs (Du

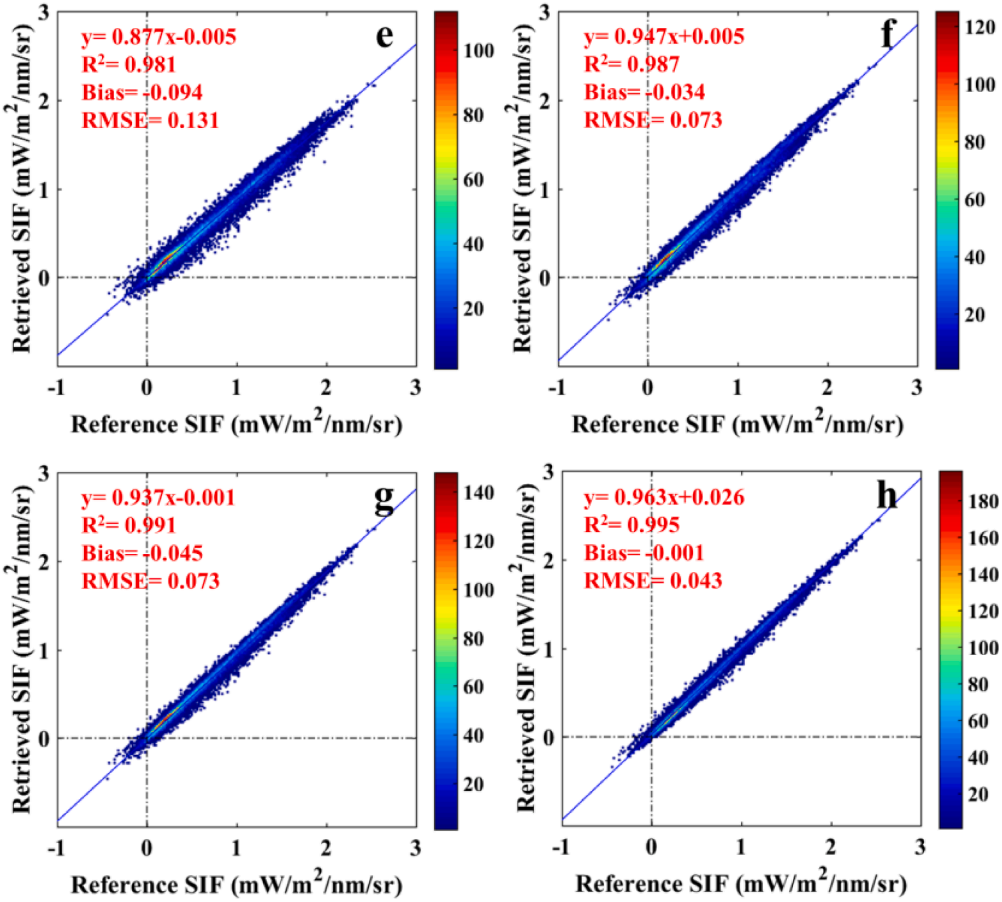

Fig. 11. (*continued*).

et al., 2018; Guanter et al., 2012). Therefore, investigations on the influence of the number of SVs on retrieval results were carried out to verify this assumption.

It should be stated that the longer the fitting window adopted by the data-driven algorithm, the more PCs are required (Köhler et al., 2015). As described in Section 4.2, SIF retrievals with more than the first four SVs are not acceptable because they have almost lost all relevance and produce a lot of negative values when compared with the reference SIF. However, compared with the number of PCs used in the PCA-based method, four is a very small number, which is related to the narrow spectral window used in this study and the longer retrieval window and complex spectral features of the PCA-based methods (Guanter et al., 2015; Joiner et al., 2013; Joiner et al., 2016). The averaged residuals (fitted radiance minus measured radiance) and RMSE between all the reconstructed radiance and measured radiance are plotted in Fig. 12. As can be seen, the averaged residuals and RMSEs are further reduced when the number of SVs used is greater than four, indicating that the spectra can be fitted well and even better when compared with that of using the first four SVs. It can be summarized that there is a limit to the number of available SVs for a retrieval window of a given length with the SVD-based approach, that when exceeded produces abnormal results. Accordingly, compared with overfitting (Guanter et al., 2012), we consider this as a form of saturation, which refers to the maximum number of SVs that can be used in a spectral window. Moreover, the findings in the study of Somkuti et al. (2021) indirectly support this conclusion by revealing that, compared with using the first four SVs, the backward elimination algorithm (Köhler et al., 2015) does not show an advantage when using narrow retrieval windows to retrieve SIF. In contrast with the PCA-based methods, that for which the retrieval results tend to be stable when the number of PCs reaches saturation (Köhler et al., 2015). The reason for this is probably that the narrow fitting window strictly limits the number of available SVs. The results in this section support the assumption made by Guanter et al. (2012) that 0.05% is an effective threshold for the SVD-based approach to select the appropriate number of SVs.

5.3. *Select an effective fitting window*

An effective fitting window is the basic requirement for accurately retrieving SIF. For the purpose of analyzing the uncertainty caused by the fitting window size, we selected micro fitting windows of 1.0–2.1 nm adjacent to the O_2-A feature, using data collected by the TanSat satellite. All these micro-windows are extremely small compared with the spectral windows (>30 nm) used in the PCA-based SIF retrieval approaches (Guanter et al., 2015; Joiner et al., 2013; Joiner et al., 2016; Köhler et al., 2015). Usually, the PCA-based SIF retrieval method is used to retrieve SIF from remote sensing data with medium spectral resolution (~0.5 nm), whereas the SVD-based SIF retrieval method is applied to satellites with ultra-high spectral resolution (<0.05 nm), e.g., TanSat, GOSAT and OCO-2.

Negative values have been a pesky problem in SIF satellite retrievals, and our analysis indicates that the main reason is due to inappropriate fitting window sizes and excessive number of SVs. We also demonstrated that other factors, such as: i) type of training set composition; ii) the spatial distribution/representativeness of the training set; and iii) the number of SVs (2–4) used in the SIF calculations, produce much lower incidences of negative values (e.g., Figs. 10 and 11) than ill-advised retrieval windows. The corresponding negative values in different figures are summarized in Table 4.

The results in Fig. 8 reveal that the fitting windows ≤ 1.3 nm introduce more undesirable negative values (Fig. 8e and f). On the contrary, the results were much improved with slightly longer windows

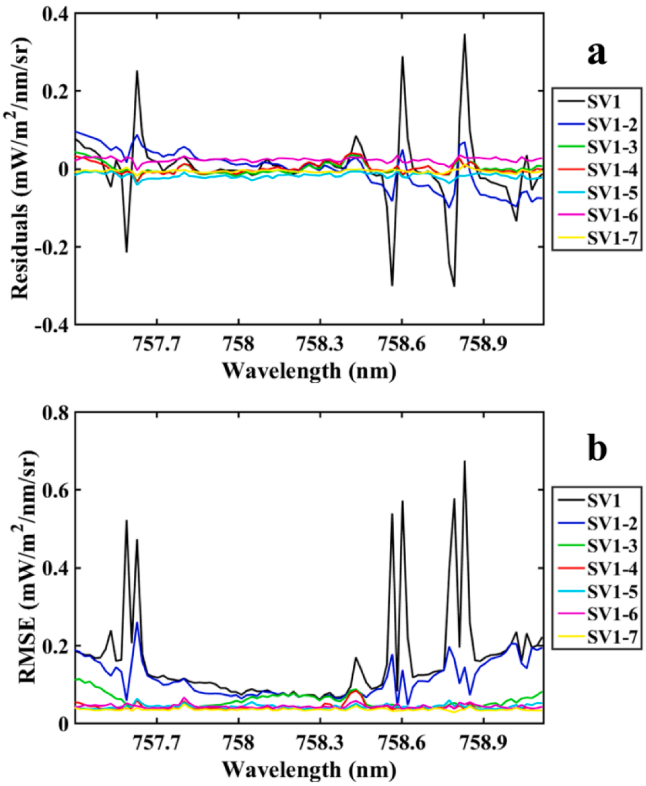

Fig. 12. Averaged residuals (a), and RMSE (b) between all the reconstructed radiance and measured radiance using the first different numbers of SVs.

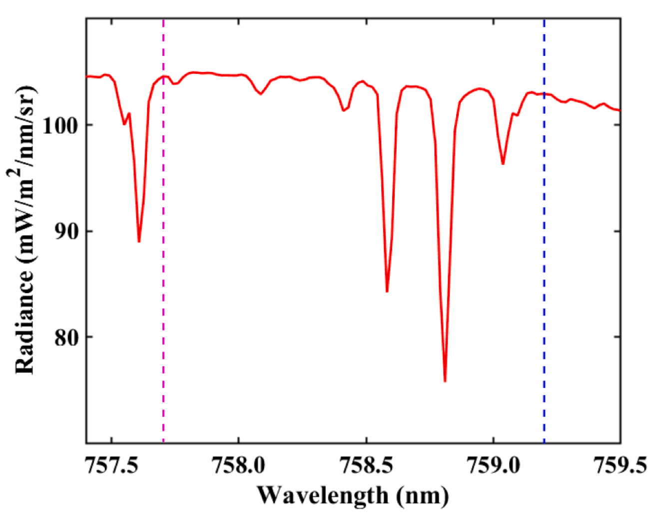

Fig. 13. An example of the fitting window. The vertical, dashed line indicate 757.7 nm (magenta) and 759.2 nm (blue). To the right of the blue line is the insertion of the wings of the O_2-A line. The closer the boundary of the spectral window to the right of the blue line, the more severely affected by the oxygen line. (For interpretation of the references to color in this figure legend, the reader is referred to the web version of this article.)

(1.5–1.9 nm, Fig. 8b–d) that contain the Fraunhofer Line at 757.6 nm. The potential evidence for this is shown in Fig. 13, where neither fitting window that yielded poor results (shown in Fig. 8e and f) contain the Fraunhofer line at 757.6 nm. This also indicates that the long spectral window should replace the short one under limited instrument conditions, such as in the study of Somkuti et al. (2021), a longer window has achieved better retrieval results. The unexpected observation is that when the fitting window is longer than the typical default length of 1.8 nm, the range of retrieved values align with the reference SIF, but their correlation is significantly reduced (Fig. 8a). This could be attributed to the weak influence of the abutting O_2-A band. Additionally, it has also been found that by increasing or decreasing the window length only slightly affects the retrieval results (Fig. 8b–d). It is encouraging to compare the latter conclusion with results found by Köhler et al. (2015) who proved that both confined and extended retrieval windows lead to a slight bias. Overall, our results provide important insights on the selection of the fitting window size centered on the Fe line at 758 nm, that is, in order to reduce unnecessary negative values, the length of the spectral window should be longer than 1.5 nm and contain several strong Fraunhofer Lines when using the SVD-based approach to retrieve SIF. As a supplement, the spectral window length at the Fe line can be extended to ~3 nm (Guanter et al., 2012; Somkuti et al., 2021), as long as it is not affected by atmospheric absorption lines. However, for TanSat satellite, the limit of the spectral window length is ~1.9 nm, because longer ones will be interfered by the oxygen lines (Fig. 8a).

Table 4
Retrieval results of different figures and their corresponding negative values. The corresponding results of Fig. 8 are presented in Table 2.

Figure	Number of negative values	Percentage of negative values	Figure	Number of negative values	Percentage of negative values
7a	4365	19.21 %	10c	733	3.23 %
7b	2411	10.61 %	10d	834	3.67 %
7c	1303	05.74 %	10e	367	1.62 %
7d	14,021	61.72 %	10f	439	1.93 %
7e	12,231	53.84 %	11a	2994	13.18 %
7f	11,797	51.93 %	11b	113	0.50 %
9a	463	2.04 %	11c	177	0.78 %
9b	309	1.36 %	11d	296	1.30 %
9c	892	3.93 %	11e	703	3.09 %
9d	300	1.32 %	11f	632	2.78 %
10a	645	2.84 %	11g	605	2.66 %
10b	748	3.29 %	11h	367	1.62 %

5.4. *Focus on the training set*

Prior studies have noted that the representativeness of the SIF-free radiance spectrum is an essential factor that significantly determines the retrieval accuracy of the data-driven SIF retrieval approach, although only a few studies have investigated the performance on this basis (Joiner et al., 2013; Köhler et al., 2015; Zhang et al., 2017). According to the literature, soil and snow spectra can be used as elements of the training set (Du et al., 2018; Guanter et al., 2012), as can sea ice, cloudy ocean, and the Sahara Desert (Joiner et al., 2016). In this study, a training set containing snow, soil, and water sites across the world was selected. Accordingly, we evaluated the impact of the type of training set elements, the proportion of training set elements, and the spatial distribution of the training set on SIF retrieval. Results showed that the first two would barely affect the retrieval results. However, the spatial distribution of the training set has a greater impact on the results, especially when the latitude coverage is small, resulting in appreciable errors (Fig. 11a). Furthermore, the current study found that even using a single element as the training set can achieve high-precision SIF retrieval. This finding, while preliminary, suggests that in the future, a single element training set (e.g., water pixels) can be selected to simplify the training set when using data-driven algorithms to retrieve SIF. It must be emphasized that based on these observations, the training set is required to be globally representative.

6. Conclusions

This study represents the first uncertainty analysis of SIF retrieval approaches using satellite measurements. The uncertainty was evaluated in terms of five aspects: the number of SVs, length of the fitting window, type of training set elements, proportion of training set elements, and spatial distribution of the training set. The main findings and suggestions are as follows:

(1) The training set should be distributed globally. Compared with the longitudinal coverage, a small latitudinal coverage (<62 latitudes) will lead to a considerable impact on SIF retrieval.
(2) The fitting window at the Fe line should be at least 1.5 nm (and up to ~3 nm) and contain several strong Fraunhofer lines, and the premise is that the window is free from the influence of atmospheric absorption lines.
(3) For the SVD-based method (within a narrow fitting window), 0.05% is an effective threshold for selecting an appropriate number of SVs.
(4) A single-element training set (e.g., N = 1) can be used for high-precision retrieval of SIF, provided that the global representation is maintained.

Declaration of Competing Interest

The authors declare that they have no known competing financial interests or personal relationships that could have appeared to influence the work reported in this paper.

Acknowledgments

This research was funded by the National Natural Science Foundation of China (grant number 41921001, 41871282) and Fundamental Research Funds for Central Non-profit Scientific Institution (No. 1610132020015).

References

Cogliati, S., Rossini, M., Julitta, T., Meroni, M., Schickling, A., Burkart, A., Pinto, F., Rascher, U., Colombo, R., 2015. Continuous and long-term measurements of reflectance and sun-induced chlorophyll fluorescence by using novel automated field spectroscopy systems. Remote Sens. Environ. 164, 270–281.
Coops, N.C., Hilker, T., Hall, F.G., Nichol, C.J., Drolet, G.G., 2010. Estimation of Light-use Efficiency of Terrestrial Ecosystems from Space: A Status Report. Bioscience 60, 788–797.
Damm, A., Guanter, L., Laurent, V.C.E., Schaepman, M.E., Schickling, A., Rascher, U., 2014. FLD-based retrieval of sun-induced chlorophyll fluorescence from medium spectral resolution airborne spectroscopy data. Remote Sens. Environ. 147, 256–266.
Damm, A., Guanter, L., Paul-Limoges, E., van der Tol, C., Hueni, A., Buchmann, N., Eugster, W., Ammann, C., Schaepman, M.E., 2015. Far-red sun-induced chlorophyll fluorescence shows ecosystem-specific relationships to gross primary production: An assessment based on observational and modeling approaches. Remote Sens. Environ. 166, 91–105.
Du, S., Liu, L., Liu, X., Zhang, X., Zhang, X., Bi, Y., Zhang, L., 2018. Retrieval of global terrestrial solar-induced chlorophyll fluorescence from TanSat satellite. Sci. Bull.
Fell, F., Fischer, J., 2001. Numerical simulation of the light field in the atmosphere-ocean system using the matrix-operator method. J. Quant. Spectrosc. Ra. 69, 351–388.
Frankenberg, C., Butz, A., Toon, G.C., 2011a. Disentangling chlorophyll fluorescence from atmospheric scattering effects in O-2 A-band spectra of reflected sun-light. Geophys. Res. Lett. 38.
Frankenberg, C., Fisher, J.B., Worden, J., Badgley, G., Saatchi, S.S., Lee, J.-E., Toon, G.C., Butz, A., Jung, M., Kuze, A., Yokota, T., 2011b. New global observations of the terrestrial carbon cycle from GOSAT: Patterns of plant fluorescence with gross primary productivity. Geophys. Res. Lett. 38.
Frankenberg, C., O'Dell, C., Berry, J., Guanter, L., Joiner, J., Köhler, P., Pollock, R., Taylor, T.E., 2014. Prospects for chlorophyll fluorescence remote sensing from the Orbiting Carbon Observatory-2. Remote Sens. Environ. 147, 1–12.
Goulas, Y., Fournier, A., Daumard, F., Champagne, S., Ounis, A., Marloie, O., Moya, I., 2017. Gross Primary Production of a Wheat Canopy Relates Stronger to Far Red Than to Red Solar-Induced Chlorophyll Fluorescence. Remote Sens-Basel 9, 97.
Grossmann, K., Frankenberg, C., Magney, T.S., Hurlock, S.C., Seibt, U., Stutz, J., 2018. PhotoSpec: A new instrument to measure spatially distributed red and far-red Solar-Induced Chlorophyll Fluorescence. Remote Sens. Environ. 216, 311–327.
Guanter, L., Aben, I., Tol, P., Krijger, J.M., Hollstein, A., Köhler, P., Damm, A., Joiner, J., Frankenberg, C., Landgraf, J., 2015. Potential of the TROPOspheric Monitoring Instrument (TROPOMI) onboard the Sentinel-5 Precursor for the monitoring of terrestrial chlorophyll fluorescence. Atmos. Meas. Tech. 8, 1337–1352.
Guanter, L., Frankenberg, C., Dudhia, A., Lewis, P.E., Gómez-Dans, J., Kuze, A., Suto, H., Grainger, R.G., 2012. Retrieval and global assessment of terrestrial chlorophyll fluorescence from GOSAT space measurements. Remote Sens. Environ. 121, 236–251.
Joiner, J., Guanter, L., Lindstrot, R., Voigt, M., Vasilkov, A.P., Middleton, E.M., Huemmrich, K.F., Yoshida, Y., Frankenberg, C., 2013. Global monitoring of terrestrial chlorophyll fluorescence from moderate-spectral-resolution near-infrared satellite measurements: methodology, simulations, and application to GOME-2. Atmos. Meas. Tech. 6, 2803–2823.
Joiner, J., Yoshida, Y., Guanter, L., Middleton, E.M., 2016. New methods for the retrieval of chlorophyll red fluorescence from hyperspectral satellite instruments: simulations and application to GOME-2 and SCIAMACHY. Atmos. Meas. Tech. 9, 3939–3967.
Joiner, J., Yoshida, Y., Vasilkov, A.P., Middleton, E.M., Campbell, P.K.E., Yoshida, Y., Kuze, A., Corp, L.A., 2012. Filling-in of near-infrared solar lines by terrestrial fluorescence and other geophysical effects: simulations and space-based observations from SCIAMACHY and GOSAT. Atmos. Meas. Tech. 5, 809–829.
Joiner, J., Yoshida, Y., Vasilkov, A.P., Yoshida, Y., Corp, L.A., Middleton, E.M., 2011. First observations of global and seasonal terrestrial chlorophyll fluorescence from space. Biogeosciences 8, 637–651.
Khosravi, N., Vountas, M., Rozanov, V.V., Bracher, A., Wolanin, A., Burrows, J.P., 2015. Retrieval of Terrestrial Plant Fluorescence Based on the In-Filling of Far-Red Fraunhofer Lines Using SCIAMACHY Observations. Front. Environ. Sci. 3.
Köhler, P., Frankenberg, C., Magney, T.S., Guanter, L., Joiner, J., Landgraf, J., 2018. Global Retrievals of Solar-Induced Chlorophyll Fluorescence With TROPOMI: First Results and Intersensor Comparison to OCO-2. Geophys. Res. Lett. 45, 10456–410463.
Köhler, P., Guanter, L., Joiner, J., 2015. A linear method for the retrieval of sun-induced chlorophyll fluorescence from GOME-2 and SCIAMACHY data. Atmos. Meas. Tech. 8, 2589–2608.
Li, S., Gao, M., Li, Z.-L., 2021. Retrieving Sun-Induced Chlorophyll Fluorescence from Hyperspectral Data with TanSat Satellite. Sensors 21, 4886.
Li, S., Gao, M., Li, Z., Li, F., Gao, Y., Liao, Q., 2018. Retrieval of chlorophyll fluorescence from Tansat in Northeast China. China Agric. Inform. 30, 53–62 (in Chinese).
Liu, X., Guo, J., Hu, J., Liu, L., 2019. Atmospheric Correction for Tower-Based Solar-Induced Chlorophyll Fluorescence Observations at O2-A Band. Remote Sens-Basel 11, 355.
Mohammed, G.H., Colombo, R., Middleton, E.M., Rascher, U., van der Tol, C., Nedbal, L., Goulas, Y., Perez-Priego, O., Damm, A., Meroni, M., Joiner, J., Cogliati, S., Verhoef, W., Malenovsky, Z., Gastellu-Etchegorry, J.-P., Miller, J.R., Guanter, L., Moreno, J., Moya, I., Berry, J.A., Frankenberg, C., Zarco-Tejada, P.J., 2019. Remote sensing of solar-induced chlorophyll fluorescence (SIF) in vegetation: 50 years of progress. Remote Sens. Environ. 231.
Porcar-Castell, A., Tyystjarvi, E., Atherton, J., van der Tol, C., Flexas, J., Pfundel, E.E., Moreno, J., Frankenberg, C., Berry, J.A., 2014. Linking chlorophyll a fluorescence to photosynthesis for remote sensing applications: mechanisms and challenges. J Exp Bot 65, 4065–4095.
Ran, Y., Li, X., 2019. TanSat: a new star in global carbon monitoring from China. Science Bulletin 64, 284–285.
Rascher, U., Alonso, L., Burkart, A., Cilia, C., Cogliati, S., Colombo, R., Damm, A., Drusch, M., Guanter, L., Hanus, J., Hyvarinen, T., Julitta, T., Jussila, J., Kataja, K., Kokkalis, P., Kraft, S., Kraska, T., Matveeva, M., Moreno, J., Muller, O., Panigada, C., Pikl, M., Pinto, F., Prey, L., Pude, R., Rossini, M., Schickling, A., Schurr, U., Schuttemeyer, D., Verrelst, J., Zemek, F., 2015. Sun-induced fluorescence - a new probe of photosynthesis: First maps from the imaging spectrometer HyPlant. Glob. Change Biol. 21, 4673–4684.
Sanders, A., Verstraeten, W., Kooreman, M., van Leth, T., Beringer, J., Joiner, J., 2016. Spaceborne Sun-Induced Vegetation Fluorescence Time Series from 2007 to 2015 Evaluated with Australian Flux Tower Measurements. Remote Sens-Basel 8, 895.
Somkuti, P., O'Dell, C.W., Crowell, S., Köhler, P., McGarragh, G.R., Cronk, H.Q., Burgh, E.B., 2021. Solar-induced chlorophyll fluorescence from the Geostationary Carbon Cycle Observatory (GeoCarb): An extensive simulation study. Remote Sens. Environ. 263, 112565.
Sun, Y., Frankenberg, C., Jung, M., Joiner, J., Guanter, L., Köhler, P., Magney, T., 2018. Overview of Solar-Induced chlorophyll Fluorescence (SIF) from the Orbiting Carbon Observatory-2: Retrieval, cross-mission comparison, and global monitoring for GPP. Remote Sens. Environ. 209, 808–823.
Wei, X., Wang, X., Wei, W., Wan, W., 2018. Use of Sun-Induced Chlorophyll Fluorescence Obtained by OCO-2 and GOME-2 for GPP Estimates of the Heihe River Basin. China. Remote Sens-Basel 10, 2039.
Wieneke, S., Ahrends, H., Damm, A., Pinto, F., Stadler, A., Rossini, M., Rascher, U., 2016. Airborne based spectroscopy of red and far-red sun-induced chlorophyll fluorescence: Implications for improved estimates of gross primary productivity. Remote Sens. Environ. 184, 654–667.
Yang, X., Tang, J., Mustard, J.F., Lee, J.-E., Rossini, M., Joiner, J., 2015. Solar-induced chlorophyll fluorescence that correlates with canopy photosynthesis on diurnal and seasonal scales in a temperate deciduous forest. Geophys. Res. Lett.
Zhang, L., Wang, S., Huang, C., 2018a. Top-of-atmosphere hyperspectral remote sensing of solar-induced chlorophyll fluorescence: A review of methods. J. Remote Sens. 22, 1–12.
Zhang, L., Wang, S., Huang, C., Cen, Y., Zhai, Y., Tong, Q., 2017. Retrieval of Sun-Induced Chlorophyll Fluorescence Using Statistical Method Without Synchronous Irradiance Data. IEEE Geosci. Remote Sens. Lett. 14, 384–388.
Zhang, Y., Guanter, L., Joiner, J., Song, L., Guan, K., 2018b. Spatially-explicit monitoring of crop photosynthetic capacity through the use of space-based chlorophyll fluorescence data. Remote Sens. Environ. 210, 362–374.